EARTH SURFACE PROCESSES AND LANDFORMS
Earth Surf. Process. Landforms **38**, 810–825 (2013)

Published online 27 September 2012 in Wiley Online Library
(wileyonlinelibrary.com) DOI: 10.1002/esp.3322

Range imaging: a new method for high-resolution topographic measurements in small- and medium-scale field sites

Manuel Nitsche,[1]* Jens M. Turowski,[1] Alexandre Badoux,[1] Dieter Rickenmann,[1] Tobias K. Kohoutek,[2] Michael Pauli[3] and James W. Kirchner[1]

[1] Mountain Hydrology and Mass Movements Unit, WSL Swiss Federal Institute for Forest, Snow and Landscape Research, Birmensdorf, Switzerland
[2] Institute of Geodesy and Photogrammetry, ETH Zurich, Switzerland
[3] Flussbau AG, Berne, Switzerland

Received 21 July 2011; Revised 3 August 2012; Accepted 22 August 2012

*Correspondence to: Manuel Nitsche, Mountain Hydrology and Mass Movements Unit, WSL Swiss Federal Institute for Forest, Snow and Landscape Research, Birmensdorf, Switzerland. E-mail: manuel.nitsche@gmail.com

ESPL
Earth Surface Processes and Landforms

ABSTRACT: Topographic measurements are essential for the study of earth surface processes. Three-dimensional data have been conventionally obtained through terrestrial laser scanning or photogrammetric methods. However, particularly in steep and rough terrain, high-resolution field measurements remain challenging and often require new creative approaches. In this paper, range imaging is evaluated as an alternative method for obtaining surface data in such complex environments. Range imaging is an emerging time-of-flight technology, using phase shift measurements on a multi-pixel sensor to generate a distance image of a surface. Its suitability for field measurements has yet not been tested. We found ambient light and surface reflectivity to be the main factors affecting error in distance measurements. Low-reflectivity surfaces and strong illumination contrasts under direct exposure to sunlight lead to noisy distance measurements. However, regardless of lighting conditions, the accuracy of range imaging was markedly improved by averaging multiple images of the same scene. For medium ambient lighting (shade) and a light-coloured surface the measurement uncertainty was approximately 9 mm. To further test the suitability of range imaging for field applications we measured a reach of a steep mountain stream with a horizontal resolution of approximately 1 cm (in the focal plane of the camera), allowing for the interpolation of a digital elevation model on a 2 cm grid. Comparison with an elevation model obtained from terrestrial laser scanning for the same site revealed that both models show similar degrees of topographic detail. Despite limitations in measurement range and accuracy, particularly at bright ambient lighting, range imaging offers three-dimensional data in real time and video mode without the need of post-processing. Therefore, range imaging is a useful complement or alternative to existing methods for high-resolution measurements in small- to medium-scale field sites. Copyright © 2012 John Wiley & Sons, Ltd.

KEYWORDS: range imaging; RIM; 3D measurements; digital elevation models; mountain streams

Introduction

High-quality surface models help to advance the understanding of earth surface processes. The rapid development of digital survey techniques in the last decade has led to a dramatic increase in terrain information and opened up new opportunities for hydrologic and geomorphologic studies (Tarolli *et al.*, 2009). However, there is still a growing need for data to document and explore the full range of spatial and temporal variability in landscapes such as river corridors (e.g. Marcus and Fonstad, 2010).

Photogrammetry and laser scanning have become widely used, and specialized workflows have been developed for obtaining three-dimensional (3D) data at various scales in diverse environments. Aerial photogrammetry has also been used over a wide range of scales, for example to measure the substrate size of gravel bed rivers (Dugdale *et al.*, 2010), to identify reach-scale gully morphology (Giménez *et al.*, 2009), and to detect debris-flow activity at the catchment scale (Berger *et al.*, 2011). Close-range applications of photogrammetry have been shown to be viable for extracting digital elevation models of small-scale roughness of exposed gravel-bed surfaces (e.g. Butler *et al.*, 1998; Lane *et al.*, 2001; Carbonneau *et al.*, 2003). Today, even consumer cameras can be employed with reasonable accuracy (few centimetres) for scientific applications (Rieke-Zapp *et al.*, 2010). To obtain a bird's eye view, digital cameras can conveniently be mounted on poles (Bird *et al.*, 2010) or kites (Giménez *et al.*, 2009), even below the forest canopy, where airborne or satellite images are not feasible. Under some circumstances, it is possible to assess the topography of submerged surfaces with multimedia photogrammetry techniques (Maas, 1995; Butler *et al.*, 2002).

Airborne laser scanning (ALS) and terrestrial laser scanning (TLS) constitute another group of measurement techniques that have been applied on a wide range of scales. TLS for example was used for small-scale measurements of weathering rates (e.g. Schaefer and Inkpen, 2010) or the characterization of

open gravel surfaces (Heritage and Milan, 2009) or other sedimentary structures (Lamarre and Roy, 2008). ALS was used for example for the recognition of channel bed morphology (Cavalli *et al.*, 2008). Moreover, protocols have been published presenting workflows for the measurement and the calculation of high-resolution elevation models on various scales, for example for rock surfaces (Schaefer and Inkpen, 2010), for alluvial river beds at grain-scale resolution (Hodge *et al.*, 2009), or for reach morphology (Heritage and Hetherington, 2007).

Even though photogrammetry and laser scanning have proven to be successful techniques to measure fluvial morphologies, high-resolution field measurements remain challenging and often require new creative approaches. In the present study we introduce range imaging (RIM) as a novel method to capture centimetre- to metre-scale surface data in the field. While laser scanning or photogrammetry is suitable for specific measurement problems, each method has its disadvantages, for example with respect to cost or weight (TLS) or with respect to processing time or surface texture (photogrammetry). RIM represents a versatile and relatively inexpensive alternative which opens up new topographic mapping possibilities in steep and rough small- to medium-scale terrain, although it cannot compensate for all the disadvantages of the other methods. One of the main advantages of RIM cameras is the possibility to acquire 3D data in real time and video mode without the need for post-processing, allowing better control over the measurements in the field.

RIM is a young but quickly developing technology. Early RIM techniques were tested and reviewed in the 1980s by Jarvis (1983) and Besl (1988). In the 1990s and early 2000s, concepts for time-of-flight solid-state range cameras were published (Schwarte *et al.*, 1995; Spirig *et al.*, 1997; Lange and Seitz, 2001) and the cameras were used in industrial applications, for example for object recognition, collision prevention, 3D modelling, mixed reality, and gesture recognition. A more recent overview of RIM cameras was given by Kolb *et al.* (2010). The suitability and accuracy of range cameras for scientific measurements has been evaluated mostly for indoor applications, for example for person height measurements (e.g. Dorrington *et al.*, 2010), and indoor distance accuracies of tens of millimetres were reported (Boehm and Pattinson, 2010). To date, there are few published applications of range cameras in the field, e.g. for scanning window frames and architectural friezes in a cultural heritage study (Chiabrando *et al.*, 2010a, 2010b), and for measuring canopy density (Schulze, 2010).

The potential of range cameras in field applications has not yet been extensively explored, and the suitability of RIM for measurements in complex and rough terrain has not been shown. The present study aims at identifying the main error sources for field RIM measurements, and quantifying the uncertainty in controlled laboratory and field measurements, expanding on the work of Nitsche *et al.* (2010). Additionally, a simple but comprehensive workflow is developed which includes field measurements, robust post-processing and the generation of a digital elevation model. As an example, we present a survey of a narrow, high-gradient mountain streambed, which provides a challenging field application with complex topography, a wide range of particle sizes, and abundant vegetation and organic material in and around the survey site. Finally, the surface model is compared to a model generated with TLS to evaluate the potential of RIM measurements.

Sources of Measurement Errors in Time-of-flight Range Cameras

Range cameras acquire 3D point clouds at video frame rates and in real time, using an indirect time-of-flight method. Their main components are an infrared signal emitter, a lens, and a sensor using Complementary Metal Oxide Semiconductor (CMOS) technology (Lange and Seitz, 2001). The emitter illuminates a scene with amplitude-modulated continuous-wave infrared light, and the reflections are projected through a lens onto a CMOS sensor. The near infrared light (850–870 nm), which is typically modulated at frequencies f_{mod} between 10 and 60 MHz, is regularly sampled at the sensor. Each sample corresponds to photo-generated charge carriers integrated over a fraction of the modulation period. Integrating multiple samples permits determination of the signal parameters intensity (I), amplitude (A) and phase (φ). The intensity I is a measure of the strength of the total light (i.e. the number of electrons per pixel generated by both the ambient light and the incoming modulated light), whereas the amplitude A is a measure of the modulation amplitude (i.e. the number of electrons per pixel generated by the incoming modulated light) (Lange *et al.*, 1999). Via an autocorrelation function the phase shift $\Delta\varphi$ between the emitted and reflected light can be detected (Möller *et al.*, 2005). The absolute target distance D being proportional to the phase shift $\Delta\varphi$ can be calculated by

$$D = \frac{c\Delta\varphi}{4\pi f_{mod}} \quad (1)$$

where c is the speed of light.

For each pixel the distance to an object is measured independently at video rate (typically 20-60 frames per second). The distance image containing the spherical distances can be transformed into a 3D Cartesian coordinate point cloud using the projection parameters of the lens. The maximum distance D_{max} that can be unambiguously measured is limited to half of the modulation wavelength λ_{mod}. At a modulation frequency of 20 MHz the modulated wavelength is 15 m and thus D_{max} is 7·5 m. Objects that are beyond D_{max} are still measured, but the distances are folded back into the non-ambiguity range, and are aliased as a distance less than D_{max} that has the same phase shift as the actual object distance.

In this study, two off-the-shelf camera models were used (Table I): the SR4000 by Mesa Imaging, Switzerland (www.mesa-imaging.ch) and the CamCube 2.0 by PMD Technologies, Germany (www.pmdtec.com). Both cameras need an external power supply and have to be connected to a computer for data acquisition.

The quality of the phase shift measurements is strongly affected by the integration time, which is the time the sensor

Table I. Range camera specifications.

	Model	
	SR4000	CamCube 2.0
Manufacturer	Mesa Imaging	PMD Technologies
Modulation frequency (MHz)	29–31	18–21
Unambiguous measurement range (m)	0·8–5	0·3–7·5
Sensor pixels	176 × 148	204 × 204
Field of view (deg)	43·6 × 34·6	40 × 40
Mean resolution at 3 m (mm)	13·6	10·7
Footprint area at 3 m (m^2)	4·48	4·77
Camera weight (g)	470	1370
Camera dimensions (mm)	65 × 65 × 68	180 × 194 × 180
Frame rate (f s^{-1})	54	25
Illumination wavelength (nm)	850	870
Price (€)	~5500	~7500

is collecting light for a single measurement. The integration time is inversely proportional to the noise in the measurements. Too long integration leads to sensor saturation, while too short integration results in a low signal-to-noise ratio (SNR). Moreover, the phase shift measurements of range cameras are susceptible to random and systematic errors, including errors originating from the optical system and the semiconductor technology itself, and errors caused by the environment, e.g. through multiple reflections and surface reflectivity properties. An error model for range imaging noise has not yet been established (Lindner *et al.*, 2010).

Internal sources of error

Scattering of light within the camera is a major error source and leads to significant distortion of the distance measurements (e.g. Kavli *et al.*, 2008; Chiabrando *et al.*, 2010a; Karel *et al.*, 2010). This effect is caused by multiple reflections between the lens, the optical filter and the sensor. As a result the light measured by each pixel is a mixture of the light reflected by the geometrically corresponding pixel footprint on the object plus a parasitic signal reflected at other pixels in the background. Scattering can cause distance errors of up to tens of millimetres, which is within the noise of range cameras (Jamtsho and Lichti, 2010). These errors increase from the sensor centre to the edges (Nitsche *et al.*, 2010). There are several methods to model and compensate scattering (e.g. Mure-Dubois and Hugli, 2007; Kavli *et al.*, 2008), and this particular source of error is not treated further within the present paper. Wiggling is another error source resulting in range dependent distance errors, and it is due to the optical signal shape that is far from the theoretically assumed sinusoidal shape (Lindner *et al.*, 2010).

The measurement accuracy is physically limited by noise generated in the range sensor itself. Primary noise types are shot noise from dark electron current dominant in low light conditions and photon-generated electron current dominant in high intensity light conditions (Büttgen *et al.*, 2005; Möller *et al.*, 2005). Furthermore, noise originates from changes in the internal temperature of the camera (Kahlmann and Ingensand, 2005; Kahlmann *et al.*, 2006; Karel *et al.*, 2010). Considering only shot noise, which cannot be reduced or eliminated by signal processing techniques, the distance accuracy can be estimated by (Lange *et al.*, 1999):

$$\sigma_D = \frac{D}{\sqrt{8}}\frac{\sqrt{I}}{A} \tag{2}$$

where σ_D is the standard deviation of the distance error, D is the target distance, I is the signal intensity and A is the signal amplitude. From Equation 2 it can be seen that measurement standard deviations are inversely proportional to the amplitude of the reflected light, which in turn is affected by the distance to the object and its reflectivity. Moreover, stronger ambient light increases the noise of the measurement.

Environmental sources of error

In addition to internal errors, many environmental factors can also contribute to measurement uncertainties. High ambient light and low surface reflectivity have been described as the main external sources of RIM error (Büttgen *et al.*, 2005; Guomundsson *et al.*, 2007). Different rock types or different degrees of surface wetness have different reflectivity, which influences the measurement accuracy (Chiabrando *et al.*, 2010b). Multipath effects can arise when backscattered light is reflected by more than one surface before reaching the sensor. This error is particularly prevalent when scanning highly reflective surfaces at close range (Guomundsson *et al.*, 2007; Karel *et al.*, 2010) or in the proximity of corners (Runne *et al.*, 2001). Multipath errors can be of any magnitude up to the maximum unambiguous range (Andrews *et al.*, 2001). Large errors can be identified and edited within the point cloud, but it is more problematic to identify small errors that occur in concave corners. Another error, referred to as 'mixed pixels' by Hebert and Krotkov (1992) may occur, when one pixel on the range sensor collects light from adjacent surfaces of different distance and the signal is integrated. Mixed pixel errors also occur in TLS measurements (Lichti *et al.*, 2005). Using full waveform analysis, like in state-of-the-art laser scanners, it would be possible to separate the first pulse reflection from any other reflections. Mixed pixels can be removed as outliers by geometric shape fitting or the use of median filters (Langer *et al.*, 2000).

More generally, the distance measurement uncertainty increases with increasing distance (MacKinnon *et al.*, 2008). Small influences of the angle of incidence on distance measurement uncertainty have been reported by Chiabrando *et al.* (2010a), and Kahlmann and Ingensand (2005). Measuring on or through translucent materials (multimedia photogrammetry) like water or glass can create additional errors (Okamoto, 1982; Maas, 1995). Light propagates slower in such materials and consequently distances are overestimated. For good conditions, i.e. high target reflectivity and little ambient light, overall distance measurement precision of about 1 cm and an accuracy up to a few centimetres has been reported in the literature (Büttgen *et al.*, 2005; Kahlmann and Ingensand, 2005; Kahlmann *et al.*, 2006; Dorrington *et al.*, 2010; Nitsche *et al.*, 2010). Manufacturers of range cameras specify an achievable accuracy of less than 1 cm (Mesa, 2011).

Quantification of Typical Errors

In the experiments described here, we quantified how distance, reflectivity and ambient light influence the uncertainty of distance measurements with the CamCube 2.0 and the SR4000 cameras (Table I), both under controlled conditions in the geodetic calibration laboratory of ETH Zürich (distance, reflectivity) and outdoors (ambient light). Some of these experiments have been previously described by Nitsche *et al.* (2010), and are summarized and supplemented here.

Experiment 1: Target distance and reflectivity

In the first experiment the precision (i.e. the repeatability) and the accuracy of distance measurements at the central pixel of the range sensor were investigated in a series of laboratory experiments for distances from 1 to 7 m. The camera was set up normal to a flat wooden board that could be moved on a calibrated rail to adjust the measuring distance (verified to within 0·2 μm with an interferometer). As a result of small flexions of the board, the adjusted camera-target distance could not be guaranteed throughout the whole surface of the board. Thus, an absolute error could only be identified to approximately ± 2 mm. Two boards were used, one black and one white, to explore two very different levels of reflectivity. The white board had an approximately eight-fold higher reflectivity in the infrared spectrum than the black board. Ambient light was turned off. For each setting the measurement was repeated 250 times. The uncertainty increased significantly with the

distance between the board and the camera (Figure 1). At 1 m the standard deviation of measured distances was 3·9 mm for the white board and 14·1 mm for the black board. At 5 m distance the standard deviation was 21·9 mm and 208·8 mm, respectively.

The distribution of the repeat measurements was approximately Gaussian (Figure 2). Only measurements on the black surface at 7 m distance showed a very different distribution with some very small distance values (Figure 2h). These were likely a result of dust particles, which created some strong early reflections, compared to the weak signal from the dark surface in the distance. The measured distances were on average overestimated when the surface was white and they were underestimated on the black surface (Figure 2).

Taking the median of multiple measurements significantly improved the accuracy compared to a single measurement. The median was preferred over the mean, because it was less sensitive to outliers or measurement errors (as seen in Figure 2h). The highest accuracy (i.e. the smallest error) was achieved for measurements at 3 m distance on the white board (1·9 mm), where accuracy was defined as the measured distance minus the independently adjusted camera-target distance. The lowest accuracy (i.e. the largest error) was observed for the black board at 5 m distance (–61·3 mm). The measurement accuracy was clearly dependent on the reflectivity of the surface: it was on average better for the white board than for the black board (Table II). Even though the measurement accuracy varied with distance, a clear functional relationship was not observed.

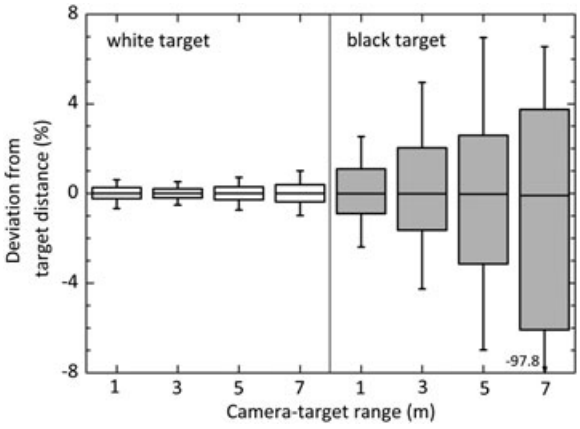

Figure 1. Relative measurement uncertainty as a function of distance for a white and a black target. Shown are data from 250 repeated measurements at the central pixel. Boxes define 25- and 75-percentile and median. Whiskers are 5- and 95-percentile of the data. Camera: CamCube, integration time 2500 μs.

Experiment 2: Ambient light

In experiment 2, the influence of ambient light on measurement quality was assessed using a flat unicoloured surface of known geometry. The measurements were performed outdoors on a white board positioned normal to the camera at approximately 3 m distance. The distance was manually adjusted using a laser distance meter, thus the assumed true distance could be identified to an accuracy of approximately ± 20 mm. For a single image of Cartesian *z*-coordinates captured in direct sunlight the standard deviation was 124·5 mm (Figure 3a, dashed lines and grey dots). Significant reduction of the standard deviation to 60·3 mm could be achieved by simple temporal averaging; here the median of 250 repeated measurements was taken (Figure 3a, straight lines and dark dots). The standard deviation was an order of magnitude smaller at night with very little ambient light: it was 13·5 mm for a single image, and 4·8 mm for the averaged data (Figure 3c). In the shade, the standard deviation was 23·2 mm for a single image and 8·5 mm for the averaged data (Figure 3b), intermediate between the results obtained in direct sunlight and night-time conditions.

Experiment 2 has shown that regardless of light conditions, averaging together multiple frames significantly reduces the uncertainty of distance measurements across the sensor, such that the random noise components of the measurement error are averaged out at each pixel. The maximum achievable reduction in per-pixel distance error depends on the number of frames. A minimum of 20 to 40 consecutive measurements was needed to achieve an improvement by a factor two to three, for both the ambient light and no ambient light experiments (Figure 4). Taking more frames did not significantly improve the image quality further. At the typical frame rates of range cameras (Table I), the time needed to acquire 50 frames is only one to two seconds.

Experiment 3: Field conditions

Real channel surfaces are much more complex than the flat, single-colour surfaces used in the tests earlier. On a natural streambed, the material reflectivity varies greatly in space and so does the measurement uncertainty. Other error sources such

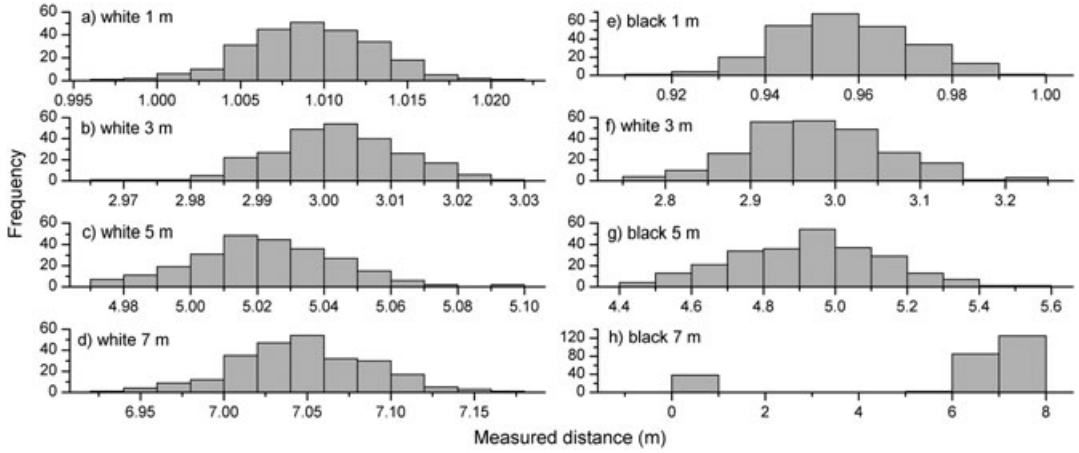

Figure 2. Histograms of distance measurements at the central pixel. Measurements from different distances were repeated 250 times each on a white (a)–(d) and a black (e)–(h) surface.

Table II. Measurement statistics for the error experiments.

Experiment	Analysed data	Number of images	Ambient light	Surface	Surface colour or reflectivity	Target distance[a] (m)	Mean measured distance (m)	Median measured distance (m)	Standard deviation (mm)	Accuracy[b] (mm)
1	central pixel	250	none	flat board	white	1·00 ± 0·002	1·0092	1·0092	3·9	9·2
	central pixel	250	none	flat board	white	3·00 ± 0·002	3·0017	3·0019	9·7	1·9
	central pixel	250	none	flat board	white	5·00 ± 0·002	5·0223	5·0228	21·9	22·8
	central pixel	250	none	flat board	white	7·00 ± 0·002	7·0474	7·0465	40·4	46·5
	central pixel	250	none	flat board	black	1·00 ± 0·002	0·9571	0·9564	14·1	–43·6
	central pixel	250	none	flat board	black	3·00 ± 0·002	2·9797	2·9730	83·4	–27·0
	central pixel	250	none	flat board	black	5·00 ± 0·002	4·9268	4·9387	209	–61·3
	central pixel	250	none	flat board	black	7·00 ± 0·002	5·9881	7·0040	2454	4·0
2	central pixel	250	direct sun	flat board	white	3·0 ± 0·02	2·9471	2·9396	183·0	–60·4
	central pixel	250	shade	flat board	white	3·0 ± 0·02	3·0009	3·0015	19·6	1·5
	central pixel	250	night	flat board	white	3·0 ± 0·02	2·9484	2·9485	11·2	–51·5
	all pixels	250	direct sun	flat board	white	3·0 ± 0·02	2·9151	2·9104	60·3	–89·6
	all pixels	250	shade	flat board	white	3·0 ± 0·02	3·0018	3·0022	8·5	2·2
	all pixels	250	night	flat board	white	3·0 ± 0·02	2·9496	2·9497	4·8	–50·3
3	several pixels	30	shade	streambed	high[c]	2·5–3·5	—	—	51·9	—
	several pixels	30	shade	streambed	medium[c]	2·5–3·5	—	—	95·8	—
	several pixels	30	shade	streambed	low[c]	2·5–3·5	—	—	179	—

[a]Independently measured distance with error margins.
[b]Defined as median measured distance minus target distance.
[c]Reflectivity class, each class indicates the relative strength of the reflected signal (cf. Figure 5).

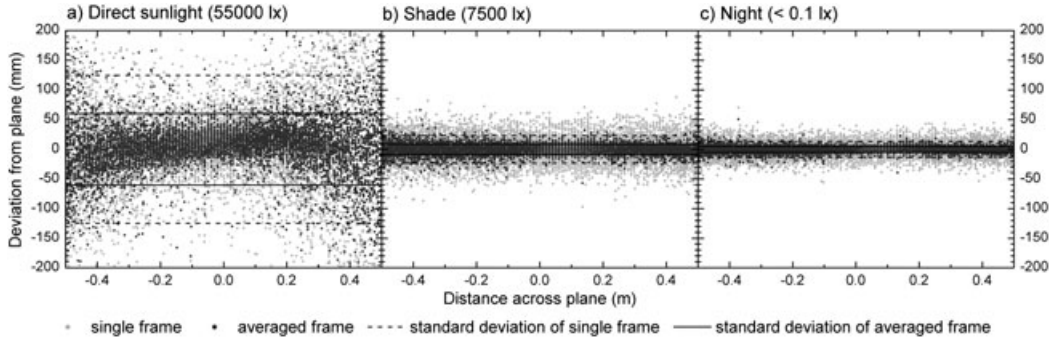

Figure 3. Uncertainty for measurements on a white plane board positioned normal to the camera at 3 m distance for different ambient light conditions. Shown are the deviations relative to a plane fitted to the measured points. The absolute position of the plane is equal to the median measured distance given in Table II. Grey dots show the vertical deviation of a single measurement from the plane position. Dark grey dots show the vertical deviation for the median of 250 repeated measurements. Lines give variability as one standard deviation. Illuminance in lux (in the visible light spectrum after CIE photopic curve) was measured with a photometer (TES Digital Illuminance Meter 1332A). Camera: CamCube, integration time 2500 µs. (a) Direct sunlight; (b) shade; (c) night.

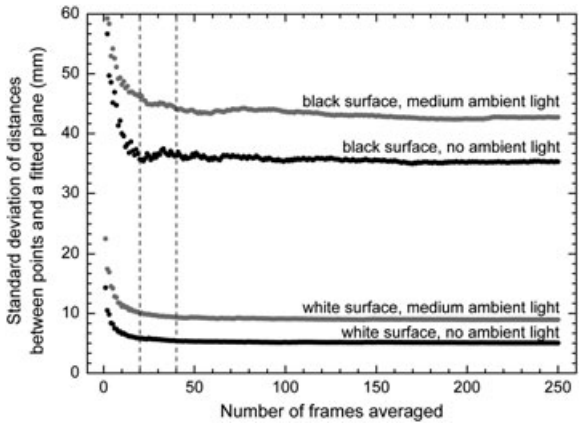

Figure 4. The effect of averaging a number of frames on the measurement uncertainty. Each frame is a distance image measured on a flat board; the white board approximately had an eight-fold higher reflectivity in the infrared spectrum than the black board. The dashed lines indicate the number of frames that must be averaged to reduce uncertainty by a factor of two to three compared to a single frame.

as surface colour contrasts, relief, and varying ambient light also affect the measurement and lead to higher uncertainty than would be observed under laboratory conditions. To assess these effects, a natural streambed surface was measured in a further experiment with range cameras looking vertically down on the channel (in a setup similar to that discussed later, see Figure 8). The obtained distance images were then classified into zones of relatively high, medium and low reflectivity, based on the signal intensity measured at the sensor. The standard deviation of distances was on average 52 mm for pixels representing highly reflective surfaces (i.e. surfaces that reflected a large portion of the emitted infrared signal) (Figure 5). For medium-reflectivity surfaces, which in our tests represented more than half of the footprint area, the standard deviation was 96 mm. Very low-reflectivity surfaces featured even larger uncertainties (Table II).

The same area was also measured under different lighting conditions, i.e. under direct sunlight at midday, in shade, and under no ambient light at night. The resulting point clouds are of very different quality (Figure 6). Night-time measurements revealed the greatest details of the surface (Figure 6b). Under

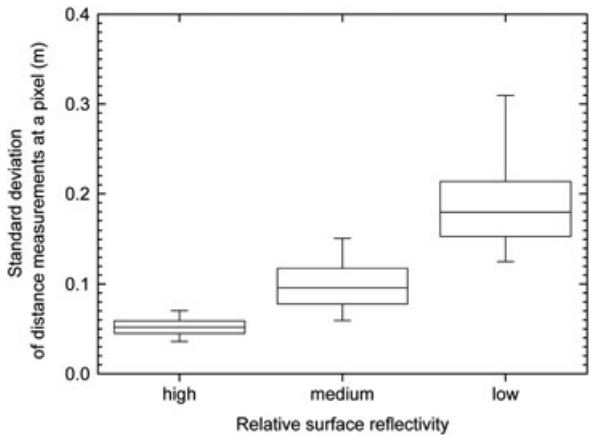

Figure 5. Measurement precision for three classes of surface reflectivity. Each class contains pixels with a defined range of 16-bit amplitude values, which indicates the strength of the reflected light (high > 400, medium 100, low < 100). For each pixel the precision is given as the standard deviation of 30 repeat distance measurements. The measurements were performed on a natural streambed surface under shady light conditions (*c.* 10 000 lx). Camera: CamCube, integration time 2500 µs.

direct sunlight exposure the point cloud became indistinct and more scattered (Figure 6d). The increased noise in the distance data is illustrated by comparing the standard deviations of measured distances from the mean surface height: the standard deviation was 0·36 m under direct sunlight, but decreased to 0·17 m under shady conditions and decreased further to 0·11 m at night. Under direct sunlight, the noise within a single measurement (in terms of distance standard deviation) was of a similar magnitude as the total surface relief (0·92 m). Water surfaces, depicted in Figure 6a, caused pronounced variations in distance measurements; turbulent water appears to cause larger measurement errors than still water surfaces. Still water permits the modulated light to penetrate and measure the underwater surface of the riverbed (although with some exaggeration of distances owing to the lower speed of light in water).

Developing a Workflow for RIM Field Data

In this section we present a workflow for (i) capturing range images in the field with the PMD CamCube camera, (ii) processing the distance data, and (iii) interpolating the 3D data to a digital terrain model (Figure 7). The test field site is also briefly introduced.

Field test site

The aim of the present study was to test range cameras in a realistically complex fluvial environment. For our test site we chose the Erlenbach, a small mountain stream located in the northern foothills of the Swiss Alps, (i) because the Erlenbach features a steep and rough streambed surface suitable to test the limits of the range cameras, (ii) because surface topography measurements for mountain streams are generally rare, and (iii) because we have validation data from a terrestrial laser scan for the Erlenbach. The study reach is about 40 m long and the mean bottom width of the channel is 3·5 m. The streambed has a mean slope of 12% and features a rough surface with a median grain size of 0·07 m and a high boulder concentration (11% of the bed surface is covered by boulders with *b*-axis diameter > 0·5 m). For more information on the Erlenbach the reader is referred to Rickenmann (1997), Hegg *et al.* (2006), and Turowski *et al.* (2009).

Fieldwork and field equipment

As with photogrammetric equipment, range cameras can be mounted and positioned using several different platforms, including cranes, balloons and drones. In the present study a

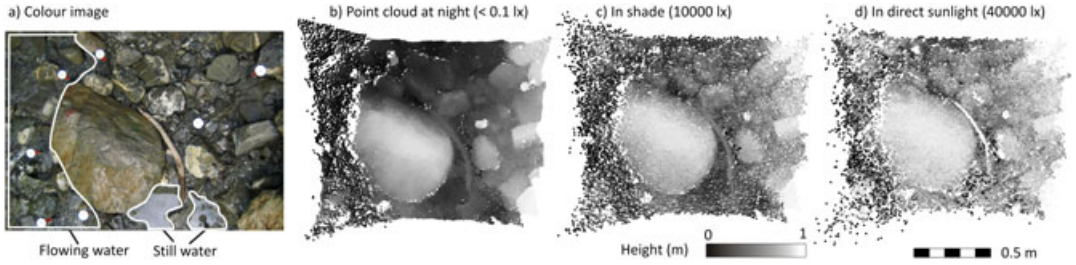

Figure 6. Colour image (a) and Cartesian coordinate points shaded by height (b)–(c) of a gravel bed surface measured under different light conditions. The mapped area is *c.* 1·6 m × 1·2 m with a density of 6 points per cm^2 near the image centre. White polygons display water surfaces. The measurements were performed under no light at night (b), in shaded daylight (c), and in direct sunlight (d). The designated heights are relative to the local minimum. Illuminance in lux was estimated from global radiation measurements. Camera: SR4000, integration time 2000 µs. This figure is available in colour online at wileyonlinelibrary.com/journal/espl

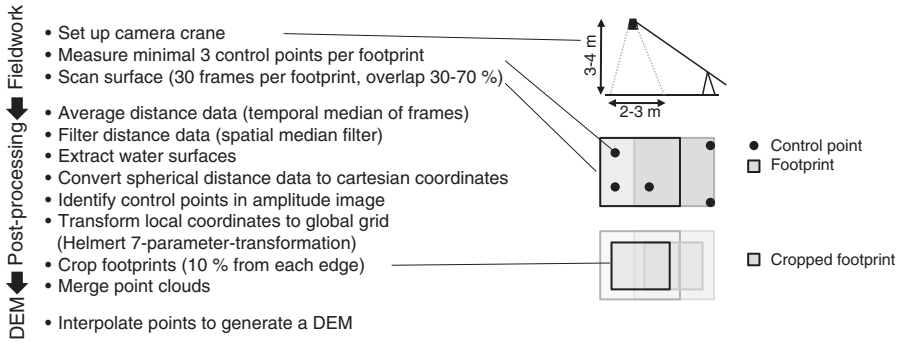

Figure 7. Workflow.

commercial lightweight camera crane with an arm length of 5·3 m was employed to provide mobility within a densely forested area, while still achieving a top-down view of the surface to minimize scan shadows (see Figure 8, Model: ABC MiniCrane 520, www.abc-products.de). Adjusting the camera height above ground controls the footprint size and the horizontal resolution of the measurements. We captured images from camera heights between 3 and 4 m with resulting footprint areas between 4·5 and 9 m^2. In total 60 footprints were taken to scan a contiguous streambed area of approximately 165 m^2. The footprints were typically overlapped by 30 to 70% to increase the point density and to guarantee seamless merging of the *xyz*-data point clouds. Additionally, three to six retro-reflective measuring nails with a diameter of 4 cm (see Figure 8) were placed per footprint and their position was surveyed independently with a total station. These control points and their local coordinates in the camera reference system were easily detectible in the camera's amplitude image (Figure 9e). This allowed for the registration of all footprints and the transformation from local camera coordinates to the Swiss coordinate system 'LV03'.

Image post-processing

The distance images taken in the field contain noise and errors of various types. While a comprehensive error model for RIM noise is unknown, noise reduction in range images is commonly done by temporal and spatial smoothing (Lindner *et al.*, 2010). We applied standard image processing methods like median filtering to remove a large portion of the errors. However, finding the optimum of the selected methods was beyond the scope of the present study. The image processing methods were rather chosen to permit a comprehensive and efficient workflow and to demonstrate the potential for data optimization. Processing was done on the distance images, i.e. on the spherical distances (D) measured with the range camera (cf. Figure 8). Cartesian coordinates were calculated after processing. Thereby one-dimensional distance errors were prevented from dispersing in the *x*-, *y*- and *z*-directions.

Temporal median

It has been shown that averaging multiple distance image frames significantly reduced the noise and thus the error of a distance image (see earlier, Figure 4). Because one frame including distance, intensity and amplitude data produces roughly one megabyte of text data, a compromise between accuracy and data volume had to be made. For each footprint we measured 30 individual frames and took the median, resulting in a significant noise reduction of the measurements (Figure 9b).

Spatial median filter

The time-averaged distance data still contained random noise, including spiky noise close to water surfaces and at the edges of the high-reflective control points (Figures 9b and 10a). Therefore, we applied a median filter, a non-linear signal processing technique which is very efficient in noise reduction (Tyan, 1981). We preferred this filter over other signal processing techniques like classical low pass filtering, because (i) it better preserves the edges of objects, (ii) it is very efficient for spiky noise and (iii) it is easy to calculate (Justusson, 1981). For each output pixel the filter calculates the median value of the neighbourhood around the corresponding pixel in the input distance image. The larger the neighbourhood (filter window) the more noise is removed, but the less edge detail is preserved. However, to remove the spiky impulses (very large positive or negative values of small spatial extent) while preserving as much edge detail as possible, the filter window has to be larger than twice the width of the impulses. Such impulses span up to three pixels in our images, thus, the optimum filter was theoretically a 7×7 pixel window. The effectiveness of the filter was visually evaluated (Figure 10). However, the performance of the chosen filter depends on the noise characteristics; thus the optimal filter size might be case-dependent.

Water surface extraction

The intensity images can be used for the detection of water surfaces. For this purpose we took advantage of the fact that water surfaces have continuously changing slopes. Even if the slope changes are very small, they affect the reflectivity of the water surface. As a result, the intensity values from water surfaces

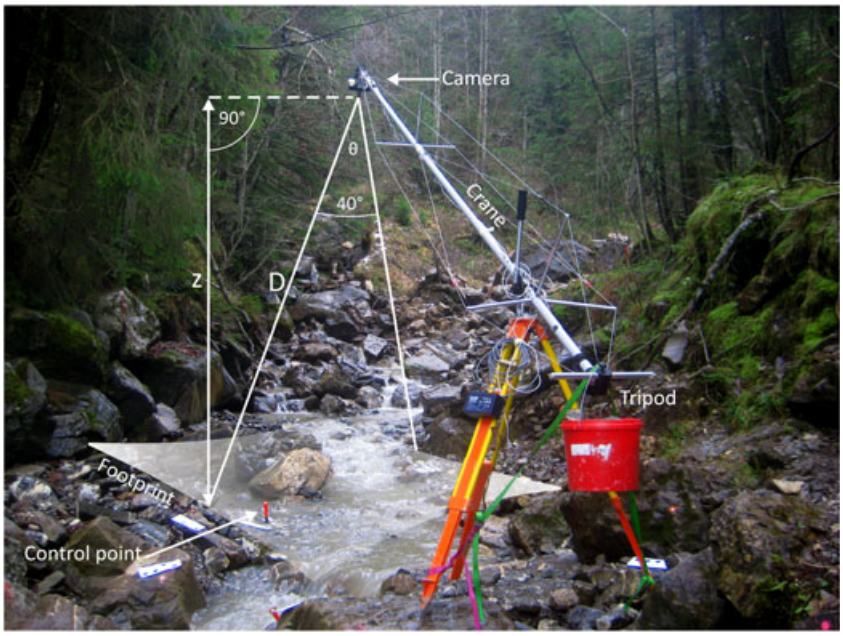

Figure 8. RIM camera setup in the Erlenbach stream: D is the measured spherical distance; z is the calculated orthogonal distance; Θ is the aperture angle of the camera; crane arm length is 5·3 m. This figure is available in colour online at wileyonlinelibrary.com/journal/espl

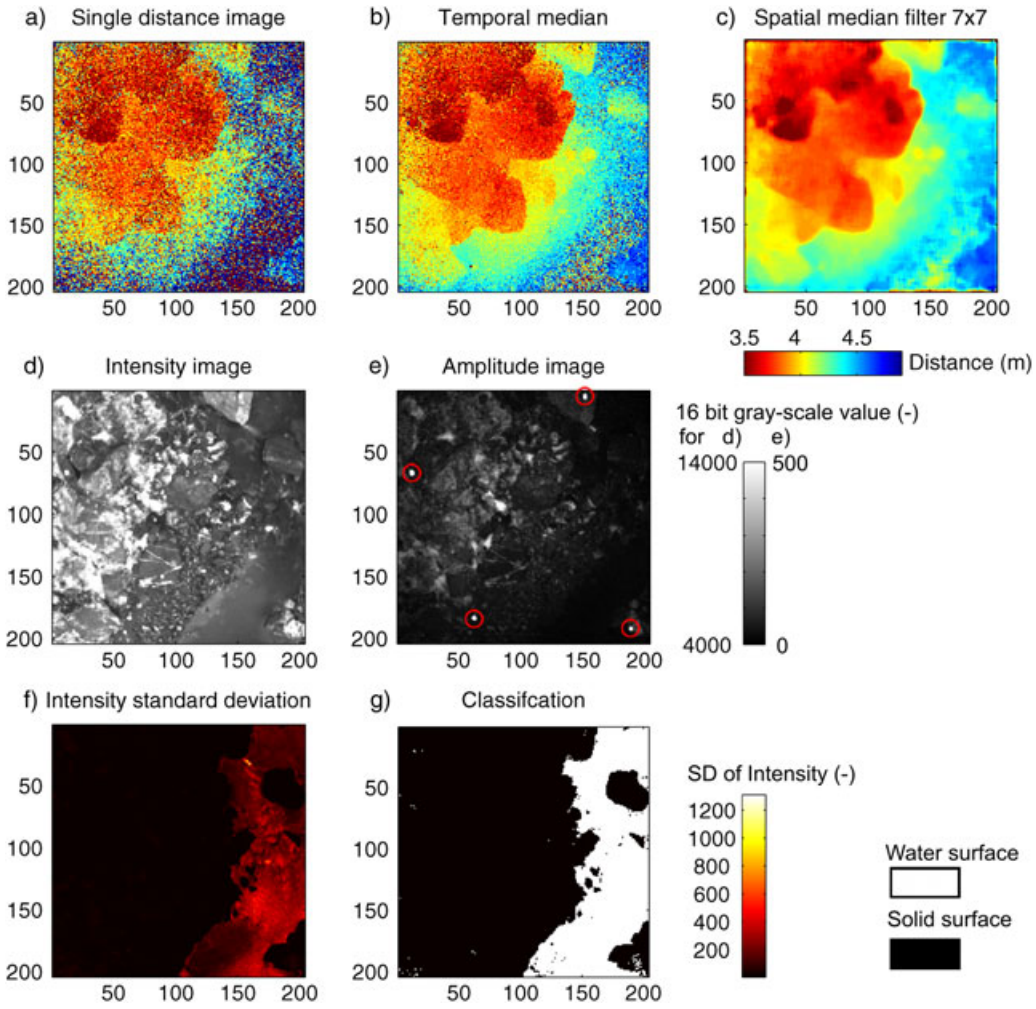

Figure 9. Processing stages and image data for an example footprint: (a) unprocessed distance image; (b) after temporal median filtering of 30 frames; (c) after spatial median filtering with a 7×7 pixel matrix. Intensity image (d), amplitude image (e). Red circles mark the position of the control points. The standard deviation of 30 frames of the intensity image (f) can be classified to distinguish water and rock surfaces (g). Axis labels denote pixel rows and columns. One pixel represents an area of approximately 1·1 cm × 1·1 cm. This figure is available in colour online at wileyonlinelibrary.com/journal/espl

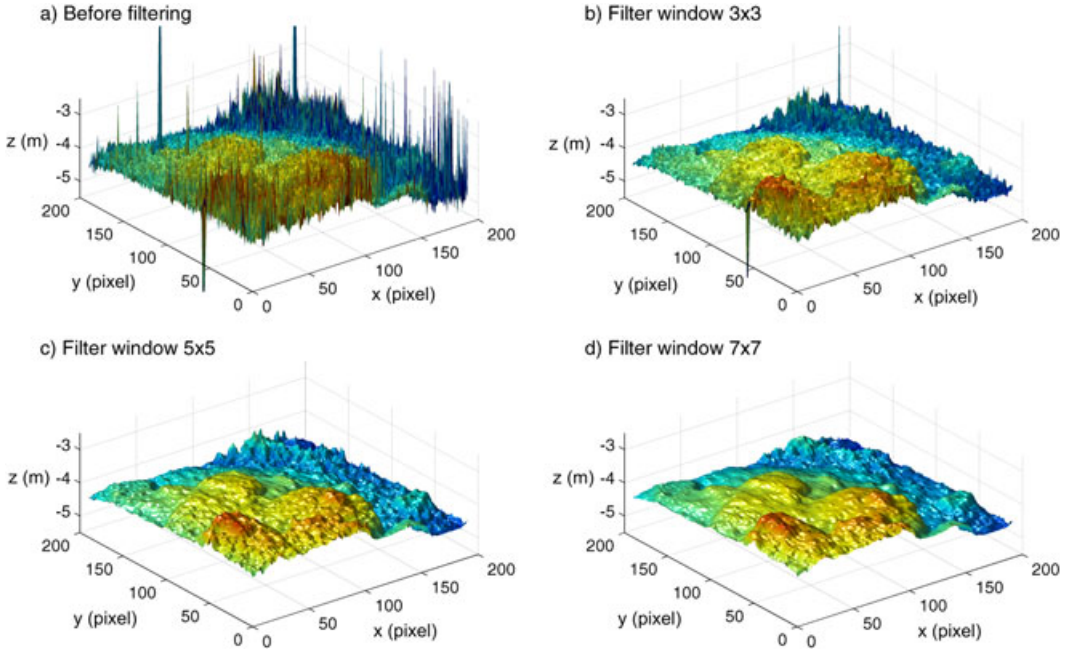

Figure 10. Three-dimensional surface plots before (a) and after (b)–(d) applying a spatial median filter to distance data of one footprint. The surfaces are shaded by height. Filter window size is given in pixels. The *x*- and *y*-axis define pixel position, *z*-axis gives distance below the camera in metres. One pixel represents an area of approximately 1·1 cm × 1·1 cm. This figure is available in colour online at wileyonlinelibrary.com/journal/espl

have a significantly larger standard deviation in time than solid rock surfaces (Figure 9f). We found that for our specific measurement setting the intensity standard deviation of solid surfaces was smaller than approximately 50 (16 bit grey scale units). Pixels with a larger standard deviation were classified as water surfaces (Figure 9g). However, the threshold between water and solid surfaces depends on the measured materials and on the light conditions and should thus be adjusted to specific site conditions.

Conversion to Cartesian coordinates
Cartesian coordinates from the processed distance images were obtained by multiplying the spherical distances by the unit vector of each pixel. Unit vectors depend on the optical characteristics of the camera and must be obtained from the internal camera memory or from the camera manufacturer.

Coordinate transformation
The Cartesian point clouds of each footprint were transformed from the local camera coordinate system to the Swiss coordinate system 'LV03'. This was achieved by applying a seven-parameter Helmert transformation using the local and the global coordinates of the control points. The coordinate transformation was performed with the triangulation software Bingo 5.5 (Geoinformatics Photogrammetric Engineering, 2011). Because of their high reflectivity, the control points and their local coordinates could be visually identified in the amplitude images (Figure 9e).

Cropping and merging point clouds
Nitsche *et al.* (2010) reported that measurements near the sensor edges are less precise than measurements in the sensor centre. Therefore, we removed 10% of the rows and columns from each edge on the sensor, which corresponds to the area on the sensor which has a distance measurement uncertainty of more than 5 mm under optimal laboratory conditions. Each cropped footprint was then merged to a stream-reach-spanning point cloud of 3D coordinates (Figure 11a).

Surface modelling
Finally, a surface model was interpolated from the processed and merged point clouds (Figure 11b) using the natural neighbour interpolation (implemented in ArcGis 9.3) at a grid spacing of 2 cm, which is about two-fold of the mean point spacing of the original point cloud. Among the large variety of interpolation techniques, the natural neighbour method (Sibson, 1981) was chosen because it was found to be an appropriate method for calculating a grid of values from data featuring a combination of regular, sparse, clustered or random distribution of points (Pirotti and Tarolli, 2010). Moreover, other interpolation or fitting techniques like kriging, splines or polynomial fitting generally result in smoother surfaces, whereas our intention was to preserve as much topographic detail as possible.

Analysis of RIM and TLS Test Measurements

Field test conditions

The range imaging data presented earlier was evaluated by comparing to TLS data collected in the same stream reach one week earlier (R. Baran, University of Munich, unpublished data). The TLS data qualifies as validation data, because the general morphology, particularly the position of larger grains and bedforms did not change between the scans. Discharge during both measurement campaigns was very low, amounting to 0·02–0·05 $m^3\ s^{-1}$ for the TLS measurement (3 November 2009) and 0·01–0·04 $m^3\ s^{-1}$ for the RIM measurement (12 November 2009), and no bedload transport was recorded between the surveys. The wetted area for the TLS and the RIM scans was 29% and 21% of the mapped area, respectively (Figures 12a and 12b). The ambient light conditions were characterized by bright diffuse light through Altostratus clouds accompanied by high contrasts. The illuminance in the visible light spectrum, estimated from global radiation data of a nearby meteorology station, was in the range of 5000 to 40 000 lx for both the RIM and the TLS measurements.

Point cloud characteristics

The point clouds of the RIM and the TLS measurements differ for example in total point number and the actual surface each point represents (Table III). The laser spot size (TLS) and the

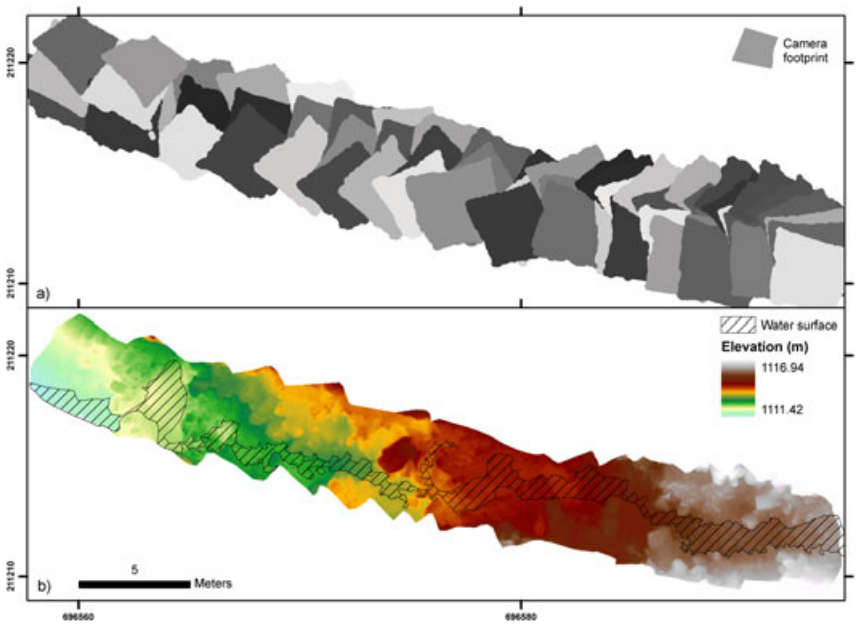

Figure 11. Top view of the study reach showing (a) RIM point clouds of the registered footprints and (b) the digital elevation model of the RIM data. This figure is available in colour online at wileyonlinelibrary.com/journal/espl

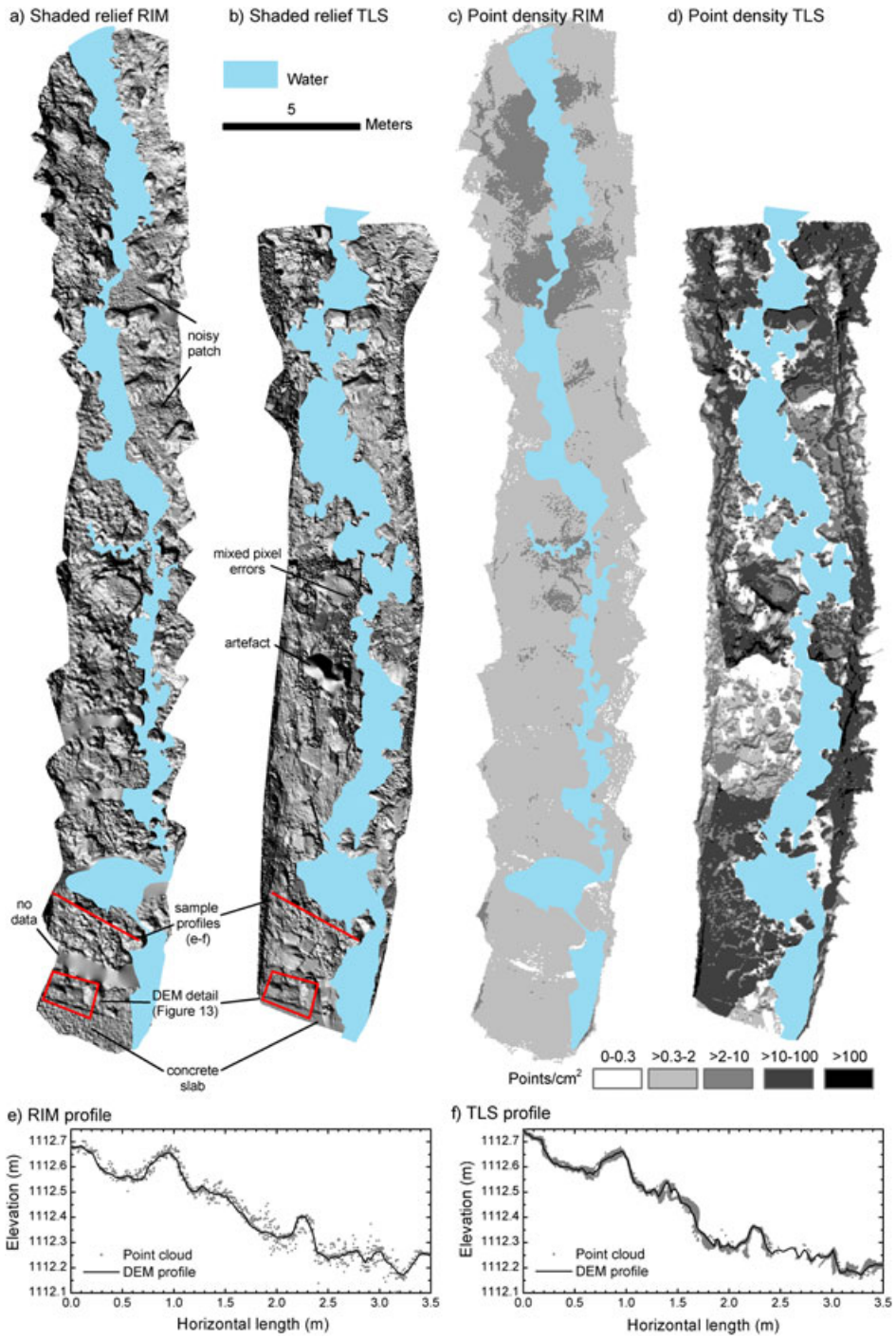

Figure 12. Shaded reliefs of digital elevation models calculated from point clouds of RIM (a) and TLS data (b), corresponding point density maps (c) and (d), and sample profiles (e) and (f). This figure is available in colour online at wileyonlinelibrary.com/journal/espl

pixel footprint (RIM) are parameters that define the smallest surface unit for which an integrated distance can be measured. The TLS laser spot has a diameter of *c.* 6 mm (at a distance of 40 m) whereas the RIM pixel side length is 11 mm (at a typical measurement range of 3 m). While the TLS measurements are made with a single laser beam at a scan rate of 3000 points per second, a single RIM measurement produces a whole distance image including more than 41 000 individual distance values. The nominal point density for TLS can be modulated, whereas point density for RIM needs to be adjusted by the distance between camera and surface or by overlapping of footprints. Points measured with RIM have a rather homogeneous, grid-like distribution over the scanned surface because the view angle is nearly vertical, whereas the point density with TLS is very heterogeneous (Figures 12c and 12d) owing to the oblique view angle and the wide range of distances between the scanner and the surface. The TLS point density was very high on surfaces perpendicularly facing the laser beam, and became very low on surfaces at shallow angles to the beam. Moreover, with the oblique view angle of TLS, many areas are in the view shade of the scanner because they are hidden behind larger objects. Due to large boulders, which hid portions of the bed even when scanning with four scan stations, 13% of the horizontally projected rock surface was effectively un-measurable. With the range camera, in comparison, only 1% of the rock surface was in the view shade, which we defined as horizontal areas with a point density of less than 0·3 points per cm^2 (Table III). However, the mean point density for RIM measurements (1·2 points per cm^2) was one order of magnitude lower than for TLS (14 points per cm^2) (Figures 12c and 12d; Table III). Both the TLS and the RIM points

Table III. Point cloud characteristics of RIM and TLS data.

	RIM	TLS
Measured area (m^2)	165	148
Pixel footprint/laser spot diameter (mm)	11×11[a]	6[b]
Mean point density (points per cm^2)[c]	1·2	14
Total point number	$2{\cdot}46 \times 10^6$	22×10^6
Size of text file with *xyz* data (Mb)	77	1660
Horizontal view shade area (%)[c,d]	1	13
Maximum registration residuals, vertical (mm)	—	7
Maximum transformation residuals, vertical (mm)	15	15

[a]At 3 m distance.
[b]At 40 m distance, after Topcon (2008).
[c]Without water surfaces.
[d]Defined by horizontal areas with a point density of $< 0{\cdot}3$ points per cm^2.

were registered and transformed into the same global coordinate system using independently measured control points (see earlier). Transformation residuals result from errors in the control point measurements as well as from errors of the point cloud itself. For both the RIM and TLS point clouds the maximum vertical transformation residuals were 15 mm (Table III). This is of the order of expected errors for the control point measurements itself, which suggests that the point clouds did not introduce significant geometric errors.

To visualize and quantify further characteristics of the RIM and TLS data, profiles (swaths) were taken from the point clouds (Figures 12a and 12b, bottom). For each sample profile all points within a distance of 1·5 cm from the profile line were analysed. The profiles of the digital elevation models along the same line are shown as a reference (Figures 12e and 12f). Both RIM and TLS point clouds match very well, with a mean elevation of 1112·43 m and 1112·42 m, respectively. However, the RIM points were more scattered around the digital elevation model profile than the TLS points, as indicated by the larger standard deviation of elevations (Table IV). The point elevations were detrended by subtracting the elevations of the respective digital elevation model profile. The resulting standard deviations of the RIM and TLS elevations are 0·026 m and 0·017 m, respectively (Table IV). The discontinuity of TLS points along the profile is a result of view shade, a problem that is insignificant for the RIM measurements due to the vertical view from above.

Digital elevation model characteristics

Digital elevation models were interpolated from the point clouds of the TLS and RIM scans. For better comparison the natural neighbour interpolation method with a grid resolution of 2 cm was applied to both datasets. The digital elevation models presented as shaded reliefs, feature a similar degree of detail (Figures 12a and 12b). Grains with a diameter larger than 10–20 cm are distinguishable throughout the RIM model. The TLS model resolves structures of approximately 10 cm in diameter. However, the TLS relief contains various interpolation artefacts, particularly in areas of little or no data (view shade). In the shaded relief of the RIM measurements some naily patterns are present, while the same areas are smooth in the TLS model (Figures 12a and 12b). These patterns are a result of the varying accuracy achieved for different footprints, visible particularly at footprint overlaps. The sample profiles of the digital elevation models suggest, that the TLS digital elevation model is more detailed in some parts, particularly where the RIM point cloud is very noisy (Figures 12e and 12f). However, on a centimetre-scale both profiles are approximately congruent. The height offsets of maximal 5 cm and a slight tilt are likely a result of registration and transformation errors (cf. Table III).

Table IV. Comparison of point clouds along a sample profile[a] (Figures 12e and 12f).

	Long profile RIM	Long profile TLS
Minimum elevation (m)	1112·097	1112·157
Maximum elevation (m)	1112·739	1112·770
Mean elevation (m)	1112·431	1112·422
Standard deviation of detrended elevations (m)[b]	0·026	0·017
Number of points	1037	11664

[a]Points in the neighbourhood (1·5 cm) of a profile line (location of profile shown in Figures 12a and 12b).
[b]Point elevations detrended by subtracting the heights of the respective digital elevation model surface.

Further quality metrics for the RIM and TLS elevation models were obtained from a digital elevation model detail (indicated in Figures 12a and 12b). The detail is located in an area where registration and transformation errors are relatively small, and these errors are not part of the comparison. Furthermore the detail covers a part of a concrete plate built in the channel, allowing for a better quality evaluation due to its known surface structure. The contour lines in the elevation are smoother in the TLS model than in the RIM model. Smooth surfaces are expected on top of the large boulder (Figures 13a and 13b, left) and the concrete plate (Figures 13a and 13b, bottom). These flat or smooth surfaces are better represented by the TLS model, whereas the RIM model shows centimetre scale distortions. While both models have the same average elevation, the RIM model features a smaller minimum elevation, a larger maximum elevation, and a larger standard deviation of elevations than the TLS model, which is again an indication for the somewhat larger uncertainty of the RIM model (Table V). The slope maps indicate how the transition from horizontal to vertical surfaces is represented in the models (Figures 13c and 13d). The narrow bands of steep slopes in the TLS model (Figure 13d, red colours) indicate a rapid transition from flat surfaces to steep grain faces. In the RIM model these transition zones are wider and also less steep. This might be due to the different footprint sizes of the laser beam and the RIM pixels. The large footprint of a RIM pixel might obscure the spatially narrow elevation changes at grain edges, because a footprint with a side length of 11 mm likely covers both grain top and bottom heights. This results in mixed pixel errors and as a consequence the grains are represented by smoother slopes. The model quality can also be evaluated by looking at the elevation variations within a defined region (here, a 3×3 pixel matrix). The RIM model on average features larger variations, suggesting the surface contains more small-scale elevation changes (Figures 13e and 13f). These small-scale changes are particularly implausible on the flat concrete plate at the bottom of the images. Thus they probably represent random errors from the RIM measurements.

Fieldwork

Time and personnel requirements were relatively similar for the RIM and the TLS campaign. The stream reach was measured within 10 hours with the RIM camera, which included crane setup, setup and measurement of control points, RIM measurements of the channel, moving the crane and packing. The work routine could probably be sped up, because this was the first attempt at field RIM measurements. The TLS measurements

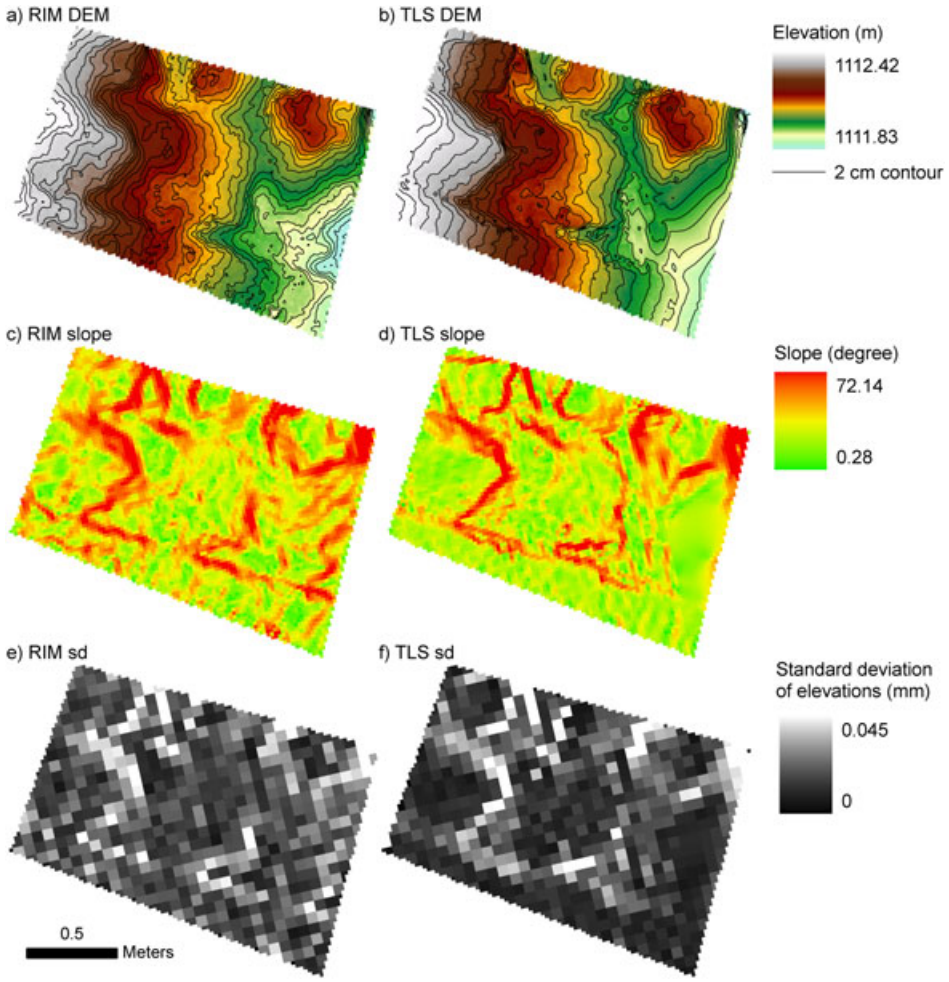

Figure 13. Details of RIM and TLS digital elevation models with a horizontal resolution of 2 cm (a) and (b), derived local slopes (c) and (d), and standard deviations of elevations within a 3×3 pixel window (e) and (f). The location of the detail is depicted in Figures 12a and 12b. This figure is available in colour online at wileyonlinelibrary.com/journal/espl

were conducted by experienced users and took seven hours, three hours less than the RIM measurements, but they covered only 90% of the RIM scan area. Both scanners were efficiently operated by two persons. For RIM measurements one person moves and positions the crane, while the other remotely controls the camera and triggers the measurements. In total 60 footprints were taken, whereas half this number would have been enough to cover the entire reach. The TLS measurements were made from four stations, each of which had to be carefully set up. Some 20 minutes are needed to scan control points and to define the scan area for each station. Depending on scan resolution, the automatic TLS scan takes minutes to several hours for each scan station. Power supply is more problematic for TLS than for RIM in remote field use. Both RIM and TLS batteries have a life time of approximately 40 minutes (Table VI). While the actual measuring time for TLS was approximately four times the battery life time, the RIM camera needs to be turned on only for a few seconds for the measurement of a footprint.

Table V. Statistics of a detail of the digital elevation models[a] (Figure 13).

	RIM digital elevation model	TLS digital elevation model
Spatial resolution (m)	0·02	0·02
Minimum elevation (m)	1111·795	1111·830
Maximum elevation (m)	1112·469	1112·418
Mean elevation (m)	1112·130	1112·130
Standard deviation of elevations (m)	0·158	0·125
Minimum slope (deg)	0·22	0·28
Maximum slope (deg)	73·59	72·14
Mean slope (deg)	26·82	23·87
Standard deviation of slope (deg)	12·35	12·55

[a]Location of the detail shown in Figures 12a and b.

Discussion

Range imaging is a method that features principles both of laser scanning and of photogrammetry. The discussion aims at identifying the major differences between the methods and assessing the potential and the limitations of range imaging in comparison to applications of TLS and photogrammetry used in the geosciences.

Data quality and spatial resolution

The tested range cameras have shown very different data quality for different ambient light conditions and reflectivity of the surface material (see earlier). In the laboratory experiments (see earlier) an accuracy of 2 to 23 mm was determined in favourable conditions (distance < 5 m, no ambient light, white surfaces) (Table II). This is in the range of values observed for photogrammetric and laser scanning techniques at similar spatial scales. An accuracy of 2 to 10 mm has been reported for photogrammetric methods (Butler *et al.*, 1998; Chandler *et al.*, 2001; Carbonneau *et al.*, 2003) and for environmental

Table VI. Field equipment and work effort for RIM and TLS test measurements in the same stream reach.

	RIM	TLS
Camera/scanner model	PMD CamCube 2·0	TOPCON GLS-1000
Measured area (m^2)	165	148
Number of footprints/stations	60	4
Scan rate (points per second)	1 040 400 (at 25 frames per second)	3000
Field personnel	2	2
Total work time in the field (hours)	10	7
Camera/scanner weight (kg)	1·4	16
Tripod weight (kg)	6·4	6·4
Camera crane weight (kg)	9	—
Netbook weight (kg)	1·2	1·2
Battery weight (kg)	2	0·4
Battery lifetime (minutes)	40 (12 V/7 Ah)	40 (7·4 V/5 Ah)
Total equipment weight without crane (kg)	11	24

applications of TLS, values from 2 to 25 mm were reported (Hetherington, 2009; Vosselmann and Maas, 2010). Hodge *et al*. (2009) observed an accuracy of approximately 2 mm for distances measured with TLS in a fluvial environment very similar to the one studied here. Under realistic conditions with shaded ambient light, the RIM accuracy is expected to be lower than observed in the laboratory. This is suggested by experiments 2 and 3 where the standard deviation of repeat measurements was relatively high and the approximate uncertainty ranged up to 52 mm (Table II). The maximal height difference in the digital elevation model profiles of the TLS and RIM data was also 50 mm (see earlier), suggesting a realistic upper limit for the RIM distance errors in the field.

Using our test camera PMD CamCube with a 204×204 pixel sensor at 3 m above the ground the spatial resolution was 11 mm. Cameras used for photogrammetry can achieve higher resolution due to their larger sensor or film resolution. Bird *et al*. (2010) for example achieved sub-centimetre resolution taking data from a distance of 10 m above ground with a non-metric film camera. The spatial resolution achievable with laser scanners depends on the distance and the angular precision (Hetherington, 2009; Vosselmann and Maas, 2010), and is limited by the size of the laser footprint. Hodge *et al*. (2009) reported a minimum footprint size of 4 mm for their TLS measurements. Assuming that an object such as a grain is identifiable when it is represented by nine equally spaced and contiguous measurements, than the smallest grain size measurable with TLS is approximately 12 mm. For our RIM test measurements the smallest grain size would be theoretically 33 mm. However, analysing the digital elevation model and the digital elevation model profiles (see earlier) the smallest identifiable grain size was in fact approximately 100 mm in diameter.

The relative geometrical stability between measured points is guaranteed by the sensor matrix for both RIM and photogrammetry techniques. This is an advantage over TLS, where the laser beam is re-positioned after each measurement (Jansa *et al*., 2004). Thus, the laser beam does not hit the exact same point twice, whereas RIM and photogrammetry measurements always capture exactly the same footprint, as long as the camera is not moved.

Post-processing and optimization

Post-processing is often a major time factor in the workflow from measurement to high quality 3D coordinates. RIM is capable of delivering 3D data in real time, without the need of post-processing. To obtain 3D coordinates in photogrammetry, a typical post-processing workflow includes calculating the orientation parameters of the images (e.g. Lindner, 2009) and measuring corresponding points (e.g. Belhumeur and Mumford, 1992). Terrestrial laser scanners deliver 3D data almost immediately after measuring. However, the large amount of data requires specialist software for registration and editing. Due to the relatively small point density in RIM measurements, the data are manageable within software environments like R and Matlab, and in geographical information systems. Nevertheless, standard image processing techniques are useful to optimize RIM data, and relatively little post-processing was required to reasonably reduce random measurement errors. We have shown that temporal averaging and spatial median filtering (see earlier) were practical and efficient in reducing the distance measurement uncertainty. In contrast, post-processing of TLS data requires somewhat greater effort and more individual filter techniques (e.g. Hodge *et al*., 2009). The simple temporal averaging and the spatial median filtering used herein are not necessarily the optimum methods. They were primarily chosen to permit a comprehensive and efficient workflow for data improvement. More sophisticated image processing methods (e.g. Gonzalez and Woods, 2002; Solomon and Breckon, 2011) might yield better results and should be investigated further. The intensity images, for example, can be used as a quality attribute of the range measurements, since higher signal intensities are proportional to measurement accuracy (MacKinnon *et al*., 2008). They can be used to detect edges and discontinuities when applying smoothing filters (Reynolds *et al*., 2011).

The calibration of digital cameras is a standard procedure in photogrammetry (Fraser, 1997). Recently, various calibration procedures have been developed that can compensate for specific systematic errors of range cameras, for example for the correction of scattering (Jamtsho and Lichti, 2010, Karel *et al*., 2010), wiggling errors (Lindner *et al*., 2010; Lichti and Kim, 2011), or errors related to reflectivity (Lindner *et al*., 2010). For the present study we calibrated the RIM cameras for interior orientation and range offsets. Other calibrations are possible, but currently there are no widely accepted strategies available.

Field and practical issues

Range cameras have some unique features that, compared to other range instruments, can facilitate measuring in the field. The 3D RIM data can be viewed in real time while measuring, which gives unique control over the scan process. Running on video mode allows for a fast collection of distance data. The 30 frames which we used for temporal averaging (cf. earlier) were collected within less than two seconds. Video mode also allows the measurement of rapidly moving surfaces, a task that laser scanners cannot currently achieve. The small size and light weight of the RIM cameras are another advantage compared to TLS. Similarly to photogrammetric cameras, RIM enables the user to mount the devices on cranes or other platforms, achieving a top view of the surface and thus preventing shading effects in many field situations.

However, the RIM method has some important practical drawbacks compared to other methods. One of the major constraints is the sensitivity to strong ambient light in the field. While it is often difficult to control the light conditions in the field (e.g. by setting up a tent over the scan area), one can compensate somewhat for the effects of strong ambient light and dark surfaces by adjusting the camera-surface distance and the integration time of the sensor, leading to a stronger signal. Laser scanners are much less sensitive to ambient light and

distance, however, direct sunlight can also affect the reflectance and lead to an erroneous signal or missing data (Charlton *et al.*, 2009). While low-light conditions are desirable for RIM and TLS measurements, photogrammetry is only possible when the surfaces are well illuminated (Jansa *et al.*, 2004). Low surface texture, shadows and severe brightness contrasts are problematic in photogrammetric applications, but have only a relatively small effect on laser scanning or RIM. Moreover, the 3D point density for photogrammetric techniques depends on the surface texture; for low-textured surfaces measurements can fail (Jansa *et al.*, 2004). In contrast, data quality is relatively independent of texture in RIM and laser scans. The range limitation of approximately 10 m restricts RIM cameras to close-range applications. Medium-range TLS scanners can measure over distances up to a few hundred metres (Charlton *et al.*, 2009), and photogrammetric cameras are generally not range-limited.

Conclusions

In the present study, RIM cameras were tested to quantify major measurement errors and to evaluate their suitability for small- to medium-scale field measurements. In addition to controlled experiments, a reach of a small, steep mountain river was measured using a RIM camera mounted on a crane. A comprehensive workflow was developed including scanning, post-processing and the calculation of a digital elevation model. Ambient light and surface reflectivity were identified as the main sources of distance measurement error. The standard deviation of repeat measurements was in the range of 9 to 52 mm for favourable field conditions, i.e. distance ≤ 5 m, shade and highly reflective flat surfaces. Higher precision was achieved when measuring without ambient light. Taking the median of repeat measurements was shown to effectively reduce random noise in the single measurements, resulting in significantly reduced distance errors. In the laboratory experiments a distance accuracy of 2 to 23 mm was determined for measurements on a highly reflective surface. For favourable field conditions the distance accuracy can be worse by a factor of two to three. However, the fast and real-time acquisition of 3D data is a main advantage compared to other available methods like laser scanning and photogrammetry. Furthermore, post-processing of RIM data, if desired, is relatively fast and straightforward. Major drawbacks of RIM include the limited range of only up to 10 m and the relatively low distance accuracy in the field due to several error sources. TLS and some photogrammetric methods are better suited for obtaining highly accurate data over long ranges. But RIM cameras are in development: with stronger signal emitters and more effective backlight suppression, range cameras will improve their target survey performance and larger sensors will allow higher horizontal resolution. Our field measurements of a river reach allowed the creation of a high-resolution (2 cm) digital elevation model, featuring a similar degree of detail as a digital elevation model created from TLS data for the same site. RIM could be considered as a substitute for terrestrial laser scanners or photogrammetric approaches in small-scale applications such as grain size diameter calculations and micro-topography measurements. Operating on video mode opens up new possibilities to study debris flows, the collapse of sand piles, or other phenomena in which surfaces evolve quickly. Positioning techniques like differential global positioning systems could be exploited and combined with range camera measurements to obtain real-time referenced global coordinates. In principle, range cameras can also be employed on a number of different platforms; for example, first experiences with RIM cameras on an unmanned helicopter have been reported by Eisenbeiss *et al.* (2011).

Acknowledgements—This study was supported by the Swiss Federal Office for the Environment (grant number 06.0083.PJ/G063-0651). The authors thank P. Thee, H. Hastedt, R. Hegglin and J. Schneider for field assistance, and B. Fritschi for crane design and technical advice. R. Baran kindly made laser scan data for the Erlenbach stream available. A. Volkwein gave support in C++ programming. The authors thank the Assistant Editor and the reviewers for detailed comments, which helped in improving this paper.

References

Andrews LC, Phillips RL, Hopen CY. 2001. *Laser Beam Scintillation with Applications*. SPIE Press: Bellingham, WA; 375.

Belhumeur PN, Mumford D. 1992. A Bayesian treatment of the stereo correspondence problem using half-occluded regions. *Computer Vision and Pattern Recognition. Proceedings CVPR '92, 1992 IEEE Computer Society Conference*; 506–512.

Berger C, McArdell BW, Schlunegger F. 2011. Sediment transfer patterns at the Illgraben catchment, Switzerland: implications for the time scales of debris flow activities. *Geomorphology* **125**(3): 421–432.

Besl PJ. 1988. Active, optical range imaging sensors. *Machine Vision and Applications* **1**: 127–152.

Bird S, Hogan D, Schwab J. 2010. Photogrammetric monitoring of small streams under a riparian forest canopy. *Earth Surface Processes and Landforms* **35**(8): 952–970. DOI: 10.1002/esp.2001

Boehm J, Pattinson T. 2010. Accuracy of exterior orientation for a range camera. *Proceedings, ISPRS Commission V Mid-Term Symposium 'Close Range Image Measurement Techniques'*, Mills JP, Barber DM, Miller PE, Newton I (eds). Newcastle upon Tyne; 103–108.

Butler JB, Lane SN, Chandler JH. 1998. Assessment of DEM quality for characterizing surface roughness using close range digital photogrammetry. *The Photogrammetric Record* **16**: 271–291.

Butler J, Lane S, Chandler J, Porfiri E. 2002. Through-water close range digital photogrammetry in flume and field environments. *The Photogrammetric Record* **17**(99): 419–439. DOI: 10.1111/0031-868x.00196

Büttgen B, Oggier T, Lehmann M, Kaufmann R, Lustenberger F. 2005. CCD/CMOS lock-in pixel for range imaging: challenges, limitations and state-of-the-art. *Proceedings, 1st Range Imaging Research Day*, Ingensand H, Kahlmann T (eds), Zürich.

Carbonneau P, Lane S, Bergeron N. 2003. Cost-effective nonmetric close-range digital photogrammetry and its application to a study of coarse gravel river beds. *International Journal of Remote Sensing* **24**(14): 2837–2854.

Cavalli M, Tarolli P, Marchi L, Dalla Fontana G. 2008. The effectiveness of airborne LiDAR data in the recognition of channel-bed morphology. *Catena* **73**(3): 249–260.

Chandler J, Shiono K, Rameshwaren P, Lane S. 2001. Measuring flume surfaces for hydraulics research using a Kodak DCS460. *The Photogrammetric Record* **17**(97): 39–61.

Charlton ME, Coveney SJ, McCarthy T. 2009. Issues in laserscanning. In *Laser Scanning for the environmental sciences*, Heritage GL, Large ARG (eds). Wiley-Blackwell: Oxford; 35–48.

Chiabrando F, Piatti D, Rinaudo F. 2010a. Integration of tof camera and multi-image matching approach for cultural heritage survey. *Proceedings, International Archives of Photogrammetry, Remote Sensing and Spatial Information Sciences, Commission V Symposium*, Mills JP, Barber DM, Miller PE, Newton I (eds), Newcastle upon Tyne.

Chiabrando F, Piatti D, Rinaudo F. 2010b. Sr-4000 tof camera: further experimental tests and first applications to metric surveys. *Proceedings, International Archives of Photogrammetry, Remote Sensing and Spatial Information Sciences, Commission V Symposium*, Mills JP, Barber DM, Miller PE, Newton I (eds), Newcastle upon Tyne.

Dorrington AA, Payne AD, Cree MJ. 2010. An evaluation of time-of-flight range cameras for close range metrology applications. *Proceedings, International Archives of Photogrammetry, Remote Sensing and Spatial Information Sciences, Commission V Symposium*, Mills JP, Barber DM, Miller PE, Newton I (eds), Newcastle upon Tyne.

Dugdale SJ, Carbonneau PE, Campbell D. 2010. Aerial photosieving of exposed gravel bars for the rapid calibration of airborne grain size maps. *Earth Surface Processes and Landforms* **35**(6): 627–639. DOI: 10.1002/esp.1936

Eisenbeiss H, Nitsche M, Kohoutek TK, Niquille P, Zander L, Ingensand H. 2011. Einsatz von autonomen Flugsystemen (UAVs) mit Distanzbildkameras in alpinen Gebieten. *Geomatik Schweiz* **109**(5): 206–208.

Fraser CT. 1997. Digital camera self-calibration. *Journal of Photogrammetry and Remote Sensing* **52**: 149–159.

Geoinformatics Photogrammetric Engineering. 2011. Bingo 5.5, Triangulation Software. http://www.gip-aalen.de/solutions.htm.

Giménez R, Marzolff I, Campo MA, Seeger M, Ries JB, Casalí J, Álvarez-Mozos J. 2009. Accuracy of high-resolution photogrammetric measurements of gullies with contrasting morphology. *Earth Surface Processes and Landforms* **34**(14): 1915–1926.

Gonzalez RC, Woods RE. 2002. *Digital Image Processing*. Prentice Hall: Englewood Cliffs, NJ.

Guomundsson SA, Aanaes H, Larsen R. 2007. Environmental effects on measurement uncertainties of time-of-flight cameras. *Proceedings, Signals, Circuits and Systems, 2007. ISSCS 2007*; 1–4.

Hebert M, Krotkov E. 1992. 3D measurements from imaging laser radars: how good are they? *Image and Vision Computing* **10**(3): 170–178. DOI: 10.1016/0262-8856(92)90068-e

Hegg C, McArdell BW, Badoux A. 2006. One hundred years of mountain hydrology in Switzerland by the WSL. *Hydrological Processes* **20**: 371–376.

Heritage G, Hetherington D. 2007. Towards a protocol for laser scanning in fluvial geomorphology. *Earth Surface Processes and Landforms* **32**(1): 66–74. DOI: 10.1002/Esp.1375

Heritage GL, Milan DJ. 2009. Terrestrial laser scanning of grain roughness in a gravel-bed river. *Geomorphology* **113**: 4–11.

Hetherington D. 2009. Laser scanning: data quality, protocols and general issues. In *Laser Scanning for the Environmental Sciences*, Heritage GL, Large ARG (eds). Wiley-Blackwell: Oxford; 82–101.

Hodge R, Brasington J, Richards K. 2009. In situ characterization of grain-scale fluvial morphology using terrestrial laser scanning. *Earth Surface Processes and Landforms* **34**: 954–968.

Jamtsho S, Lichti DD. 2010. Modelling scattering distortion in 3d range camera. *Proceedings, International Archives of Photogrammetry, Remote Sensing and Spatial Information Sciences, Commission V Symposium*, Mills JP, Barber DM, Miller PE, Newton I (eds), Newcastle upon Tyne.

Jansa J, Studnicka N, Forkert G, Haring A, Kager H. 2004. Terrestrial laser scanning and photogrammetry – acquisition techniques complementing one another. *Proceedings, XXth ISPRS Congress*, Istanbul.

Jarvis RA. 1983. A perspective on range finding techniques for computer vision. *IEEE Transactions on Pattern Analysis and Machine Intelligence* **5**(2): 122–139.

Justusson B. 1981. Median filtering: statistical properties. In *Two-dimensional Digital Signal Processing II. Topics in Applied Physics*, Huang TS (ed.). Springer: Berlin; 161–196.

Kahlmann T, Ingensand H. 2005. Range imaging sensor properties and calibration. *Proceedings, 1st Range Imaging Research Day*, Zurich.

Kahlmann T, Remendino F, Ingensand H. 2006. Calibration for increased accuracy of the range imaging camera Swiss ranger. *TM Proceedings of the ISPRS Commission V Symposium*, Dresden.

Karel W, Ghuffarb S, Pfeiferb N. 2010. Quantifying the distortion of distance observations caused by scattering in time-of-flight range cameras. *Proceedings, International Archives of Photogrammetry, Remote Sensing and Spatial Information Sciences, Commission V Symposium*, Mills JP, Barber DM, Miller PE, Newton I (eds), Newcastle upon Tyne.

Kavli T, Kirkhus T, Thielemann JT, Jagielski B. 2008. Modelling and compensating measurement errors caused by scattering in time-of-flight cameras – art. no. 706604. In *Two- and Three-dimensional Methods for Inspection and Metrology VI*, Huang PS, Yoshizawa T, Harding KG (eds), Proceedings of the Society of Photo-optical Instrumentation Engineers (SPIE). SPIE Press: Bellingham, WA.

Kolb A, Barth E, Koch R, Larsen R. 2010. Time-of-flight cameras in computer graphics. *Computer Graphics Forum* **29**(1): 141–159.

Lamarre H, Roy AG. 2008. A field experiment on the development of sedimentary structures in a gravel-bed river. *Earth Surface Processes and Landforms* **33**: 1064–1081.

Lane SN, Chandler JH, Porfiri K. 2001. Monitoring river channel and flume surfaces with digital photogrammetry. *Journal of Hydraulic Engineering ASCE* **127**(10): 871–877.

Lange R, Seitz P. 2001. Solid-state, time-of-flight range camera. *IEEE Journal of Quantum Electronics* **37**(3): 390–397.

Lange R, Seitz P, Biber A, Schwarte R. 1999. Time-of-flight range imaging with a custom solid-state image sensor. In *Laser Metrology and Inspection*, Tiziani HJ, Rastogi PK (eds). SPIE Press: Bellingham, WA; 180–191.

Langer D, Mettenleiter M, Härtl F, Fröhlich C. 2000. Imaging Ladar for 3-D surveying and CAD modeling of real-world environments. *International Journal of Robotics Research* **19**(11): 1075–1088. DOI: 10.1177/02783640022067986

Lichti DD, Kim C. 2011. A comparison of three geometric self-calibration methods for range cameras. *Remote Sensing* **3**(5): 1014–1028. DOI: 10.3390/rs3051014

Lichti DD, Gordon SJ, Tipdecho T. 2005. Error models and propagation in directly georeferenced terrestrial laser scanner networks. *Journal of Surveying Engineering – ASCE* **131**(4): 135–142. DOI: 10.1061/(asce)0733-9453(2005)131:4(135)

Lindner W. 2009. *Digital Photogrammetry*. Springer: Berlin.

Lindner M, Schiller I, Kolb A, Koch R. 2010. Time-of-flight sensor calibration for accurate range sensing. *Computer Vision and Image Understanding* **114**(12): 1318–1328. DOI: 10.1016/j.cviu.2009.11.002

Maas HG (ed.). 1995. *New Developments in Multimedia Photogrammetry. Optical 3-D Measurement Techniques III*. Wichmann: Heidelberg.

MacKinnon D, Aitken V, Blais F. 2008. Review of measurement quality metrics for range imaging. *Journal of Electronic Imaging* **17**(3): 14. DOI: 10.1117/1.2955245

Marcus WA, Fonstad MA. 2010. Remote sensing of rivers: the emergence of a subdiscipline in the river sciences. *Earth Surface Processes and Landforms* **35**(15): 1867–1872. DOI: 10.1002/esp.2094

Mesa. 2011. *SR 4000 User Manual*. Mesa Imaging: Zürich.

Möller T, Kraft H, Frey J, Albrecht M, Lange R. 2005. Robust 3D measurements with PMD sensors. *Proceedings, 1st Range Imaging Research Day*, Zurich.

Mure-Dubois J, Hugli H. 2007. Optimized scattering compensation for time-of-flight camera – art. no. 67620H. In *Two- and Three-dimensional Methods for Inspection and Metrology V*, Huang PS (ed.), Proceedings of the Society of Photo-Optical Instrumentation Engineers (SPIE). SPIE Press: Bellingham, WA; H7620–H7620.

Nitsche M, Turowski J, Badoux A, Pauli M, Schneider J, Rickenmann D, Kohoutek T. 2010. Measuring streambed morphology using range imaging. In *River Flow 2010*, Dittrich A, Koll K, Aberle J, Geisenhainer P (eds). Bundesamt für Wasserbau: Braunschweig; 1715–1722.

Okamoto A. 1982. Wave influences in 2-media photogrammetry. *Photogrammetric Engineering and Remote Sensing* **48**(9): 1487–1499.

Pirotti F, Tarolli P. 2010. Suitability of LiDAR point density and derived landform curvature maps for channel network extraction. *Hydrological Processes* **24**(9): 1187–1197. DOI: 10.1002/Hyp.7582

Reynolds M, Dobos J, Peel L, Weyrich T, Brostow GJ. 2011. Capturing time-of-flight data with confidence. *Proceedings, Computer Vision and Pattern Recognition (CVPR), 2011 IEEE Conference*; 945–952.

Rickenmann D. 1997. Sediment transport in Swiss torrents. *Earth Surface Processes and Landforms* **22**: 937–951.

Rieke-Zapp DH, Bommer-Denss B, Ernst D. 2010. Small format digital photogrammetry for applications in the earth sciences. *Proceedings, ISPRS Commission V Mid-Term Symposium 'Close Range Image Measurement Techniques'*, Mills JP, Barber DM, Miller PE, Newton I (eds), Newcastle upon Tyne; 516–519.

Runne H, Niemeier W, Kern F. 2001. Application of laser scanners to determine the geometry of buildings. *Proceedings, Optical 3-D Measurement Techniques IV*, Wien; 41–48.

Schaefer M, Inkpen R. 2010. Towards a protocol for laser scanning of rock surfaces. *Earth Surface Processes and Landforms* **35**(4): 147–423.

Schulze M. 2010. 3D-camera based navigation of a mobile robot in an agricultural environment. *Proceedings, International Archives of Photogrammetry, Remote Sensing and Spatial Information Sciences, Commission V Symposium*, Mills JP, Barber DM, Miller PE, Newton I (eds), Newcastle upon Tyne.

Schwarte R, Heinol H-G, Xu Z, Hartmann K. 1995. New active 3D vision system based on rf-modulation interferometry of incoherent light. In *Intelligent Robots and Computer Vision XIV: Algorithms, Techniques, Active Vision, and Materials Handling*. SPIE Press: Bellingham, WA; 126–134.

Sibson R. 1981. A brief description of natural neighbor interpolation. In *Looking at Multivariate Data*, Barnett V (ed.). John Wiley & Sons: Chichester; 21–36.

Solomon C, Breckon T. 2011. *Fundamentals of Digital Image Processing: A Practical Approach with Examples in Matlab*. John Wiley & Sons: Chichester.

Spirig T, Marley M, Seitz P. 1997. The multitap lock-in CCD with offset subtraction. *IEEE Transactions on Electron Devices* **44**(10): 1643–1647.

Tarolli P, Arrowsmith JR, Vivoni ER. 2009. Understanding earth surface processes from remotely sensed digital terrain models. *Geomorphology* **113**(1–2): 1–3.

Topcon. 2008. *LaserScanner GLS-1000, Spec Sheet*. Topcon Corporation: Tokyo.

Turowski JM, Yager EM, Badoux A, Rickenmann D, Molnar P. 2009. The impact of exceptional events on erosion, bedload transport and channel stability in a step-pool channel. *Earth Surface Processes and Landforms* **34**: 1661–1673.

Tyan S. 1981. Median filtering: deterministic properties. In *Two-Dimensional Digital Signal Processing II. Topics in Applied Physics*, Huang TS (ed.). Springer: Berlin; 197–217.

Vosselmann G, Maas H-G (eds). 2010. *Airborne and Terrestrial Laser Scanning*. Whittles: Caithness.